Estimation of geomechanical properties by use of combined CT-scan and XRD analysis (Digital Rock Physics)

K-Hosseini, B.

Saskatchewan Research Council, Regina, Canada

ABSTRACT: The Geomechanical characterization of reservoir rocks is quite important in petroleum geomechanics applications. Obtaining the geomechanical properties is usually an expensive component of geomechanical studies, as it requires sampling and running intensive lengthy rock mechanics tests. Information from combined rock physics and log data are also useful sources in geomechanical characterization of reservoir rocks. However, for horizontal wellbores, sampling core plugs in all locations along the wellbore is impossible. Rock mechanics tests are commonly destructive tests, and 3D geomechanical models are also uncertain as there is little hard data (vertical wellbore logs, cores and image logs) to support the spatial geomechanical distribution. This study provides a new approach on estimation of geomechanical properties by CT scan image segmentation analysis and X-ray diffraction. The elastic properties are mainly linked to the composite mineralogy of the minerals that form the rock. In this study, the rock mechanics properties obtained from drained triaxial rock mechanics tests were compared against their weight percent of different minerals in sand and clay lenses. Various properties such as uniaxial compressional strength and tensile strength of the rock samples showed a correlation to their weight and volume fraction of the minerals at the plane of failure under triaxial loading. XRD analyses were conducted at the plane of failure, post the failure of the rock under loading. CT scan-based segmentation of the rock samples pre and post failure on the bulk volume of core plugs were analyzed to find their relationship with the geomechanical properties. The constructed correlations and cross-plots can help in estimating the properties of the geomechanical properties in other locations in the same geological zone (i.e. along a horizontal wellbore) by having the rock mechanics test results in a few locations in the reservoir. The methodology was tested on core samples of a field in western Saskatchewan, Canada. This technique provides insight and a rough estimate of elastic and constitutive rock properties without destructing the rocks.

1. INTRODUCTION

One of the influential parameters for development and completion and production from horizontal wellbores are the geomechanical properties of the formation rock. In some applications, such as hydraulic fracturing, the essential parameters to evaluate the success of potential stimulation jobs are elastic geomechanical rock properties such as Young Modulus and Poisson's Ratio. During flooding processes in tight and conventional formations, geomechanics can play a significant role in performance of flooding (Koohmareh Hosseini and Chalaturnyk, 2014) since flooding changes porosity and permeability dynamically, and the flooding induced fractures (Settari

and Warren, 1994) in brittle formations can change the sweep efficiencies or cause early breakthrough. In environmental footprints related to oil and gas, such as Steam Assisted Gravity Drainage (SAGD) and induced seismicity related to fault reactivation (K. Hosseini and Eaton, 2018), knowing the geomechanical properties is quite crucial in the assessment of process performance or controlling the operational parameters to mitigate any hazard. However, reservoir and geomechanical characterizations are performed mostly locally on the extracted core samples at the well level, and obtaining the data require performing destructive test on the core, which makes the process expensive and impossible in some cases when core is not available. Development of a

methodology to characterize geomechanical properties (like Young Modulus and Poisson's Ratio) in a larger space such as along the trajectory of a horizontal wellbore, and without destructing the samples will not only minimize the cost of characterization, but also will improve the performance of the oil and gas operations that require geomechanical analysis and evaluation.

The significance of compositional control on estimation and prediction of geomechanical properties has been the subject of few studies in the past (Vaisblat et al., 2019). Use of petrography in the estimation of rock mechanical properties such as "brittleness" has been the area of studies in a few recent works including Katz et al., 2016, that analyzed the rock brittleness by use of QEMSCAN on a Niobrara formation core study. The analysis of thin section for estimation of geomechanical properties was used in a study by Saxena and Mavko, 2016. Saxena and Mavko, 2016, and Saxena et al., 2017, estimated 3D elastic rock moduli and permeability from 2D images (2016). In their study, thin sections were extracted from each 3D volume, and the computed moduli from thin sections were used in a power law form of equation to estimate the 3D bulk volume.

This study not only uses rock minerals' compositional data from XRD (X-Ray Diffraction), but also combines that with data obtained from petrography method such as QEMSCAN (Quantitative Evaluation of Materials by Scanning) to evaluate the geomechanical properties at the 2D level, and uses CT-scan imagery combined with deep learning-based segmentation techniques to evaluate the properties at the 3D level. Use of this workflow is very novel and the results support the practicality of the methodology.

The Viking formation has large compositional variation in clay content and distribution, and poor cementing, which makes it a good potential subject for investigation of relationships between rock composition and the geomechanical properties of the formation.

2. TRIAXIAL ROCK MECHANICAL TESTING

A 4-stage drained triaxial test was conducted using static confining pressures of PC1=2 MPa, PC2=3 MPa, PC3=5 MPa and PC4=7 MPa. The samples were labelled as sample 2, 8, 11, 16 and 17. Table 1 summarizes the computed elastic properties for these five core samples at a confining pressure of 7 MPa.

Table 1. Triaxial drained rock mechanics test data

Sample ID	Depth (m)	Confining Pressure (MPa)	Compressive Strength $(\sigma_d + P_c)$ (MPa)	Static Young's Modulus (GPa)	Static Bulk Modulus (GPa)	Static Shear Modulus (GPa)	Hydrostatic Bulk Modulus (GPa)
2	701.15	7.0	59.91	6.31	2.79	2.81	4.55
8	702.17	7.0	59.94	6.19	2.61	2.80	4.15
11	702.78	7.0	69.08	9.07	4.85	3.82	4.27
16	703.50	7.0	55.56	6.65	3.94	2.73	3.64
17	703.57	7.0	63.01	9.59	4.95	4.07	4.75

Samples 11, 16, and 17 were loaded at various confining pressures, whereas samples 2 and 8 were loaded only at effective confining pressure of 7 MPa. Also, Poisson's Ratio was measured in two different directions using the cantilever diametral deformation device that measured deformations in both orthogonal directions x and y. The LVDTs measured displacement in the axial z direction. The raw and shifted stress values are separated, and Uniaxial Compressive Strength (UCS), cohesion and friction angle were calculated at both "raw" and "shifted" values. The term "shifted" is used to account for the underestimated cohesion values in the multi-stage laboratory load testing. Since the stage is switched as dilation occurs, the compressive strengths of stages prior to the last stage are underestimated. To correct for the underestimation, the ratio of the maximum principal stress at dilation to maximum stress during the final stage is applied to the previous stages, while keeping the minimum principal stress σ_3 constant.

In one approach, the yield envelope of all core samples that were collected at different depths were combined to obtain an average yield envelope for the entire reservoir. However, a more accurate analysis involves obtaining the yield envelope for each location in the formation (rock test sample) separately, because different locations in the reservoir have different elastic and plastic behaviour. Samples 11, 16 and 17 were analyzed separately and the Mohr-Coulomb envelopes were calculated for them individually. Each stage in the multi-stage test represents one circle in the yield envelope and by combining all the Mohr-Coulomb circles, one can obtain the "average" cohesion and friction angle of the rock. Fig. 1 and Fig. 2 represent the result for sample #16 for all four different stages, at both pre-peak and post-failure states.
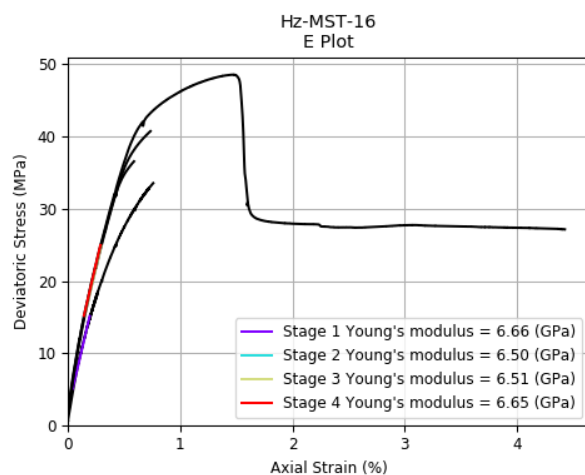
Fig. 1. Deviatoric stress versus axial strain during drained multi-stage triaxial test. Young Modulus at each confining pressure (stage) is calculated from the slope of the curve.
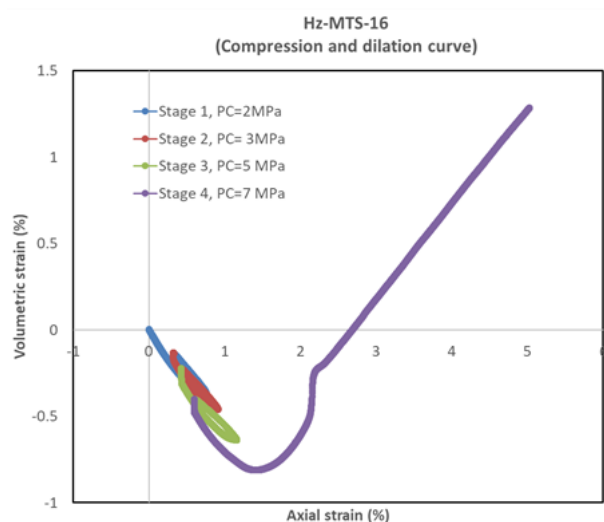

Fig. 2. Volumetric strain versus axial strain during drained multi-stage triaxial test on sample #16 for various confining pressures. Average Poisson's Ratio can be computed from this curve at each stage.

3. MINERALOGICAL COMPOSITION

The mineralogical compositions were obtained by analyzing the five core samples of one well in the Kerrobert area Viking formation using both XRD and QEMSCAN analysis. Both analyses were performed on the plane of failure, where the rock sheared at an angle with respect to maximum principal stress in the triaxial drained test.

XRD analysis represents only one single pinpoint location of the rock sample, but it provided a good guideline for the further QEMSCAN analysis. XRD showed the existing dominant sand minerals are "quartz" and "feldspars". Feldspar minerals include K-feldspar and Na-feldspar (plagioclase). The XRD derived clay minerals include "illite", "smectite" and an interbedded layer of "illite-smectite" (Fig. 3). The clay portion of the

rock was separated from the sand portion by the grain size; Any grain that was smaller than 5 µm was considered as clay.

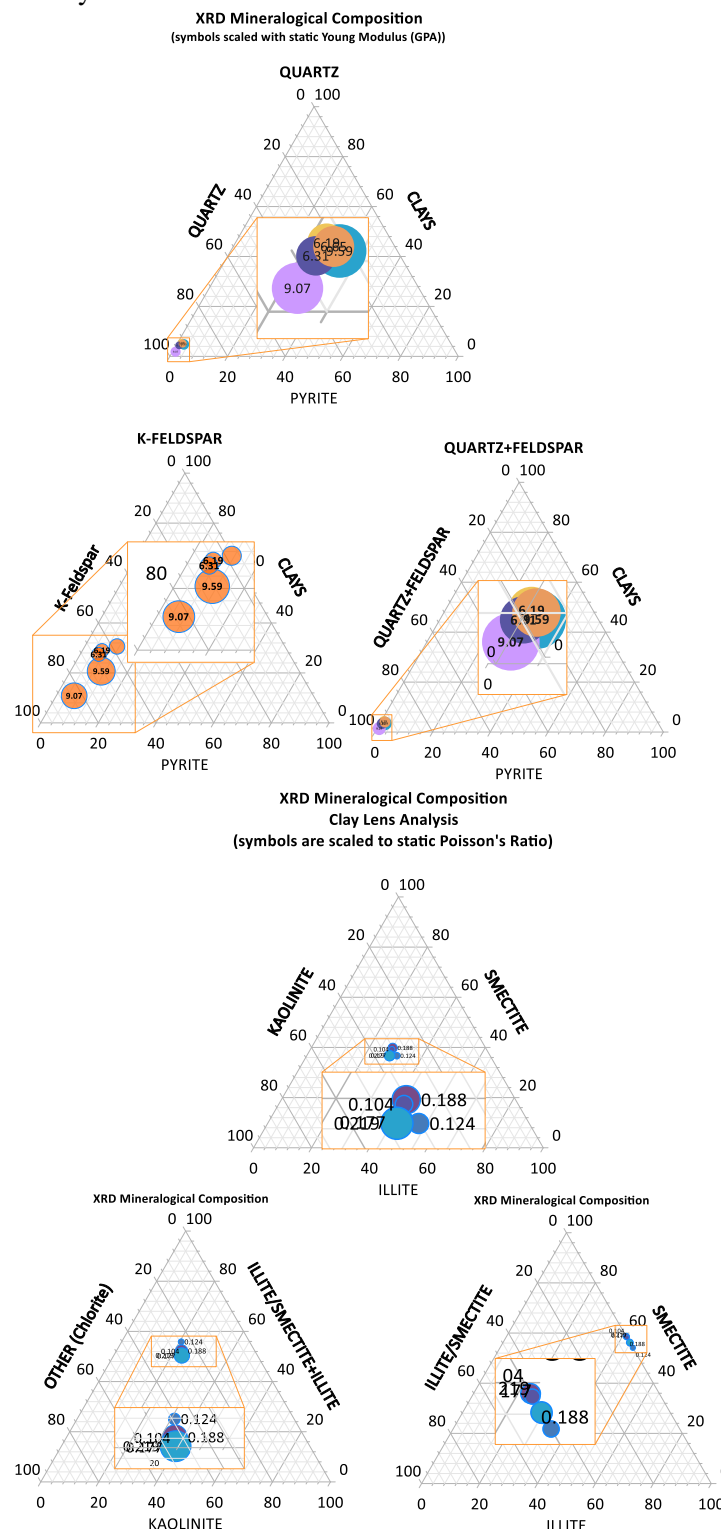Fig. 3. Mineralogical composition of a well in the Kerrobert area Viking formation, obtained by XRD analysis of five core samples from one well. The top three ternary diagrams show overall XRD composition of the core samples (bubble sizes are scaled to Young Modulus) and the lower three ternary diagrams illustrate only the clay lens portion of the core samples (bubble sizes are scaled to Poisson's Ratio).

The numbers in part (b) of Fig. 3 refer to the clay minerals and are normalized to 100% in the clay lens only.

The QEMSCAN analysis showed the presence of some mica (<1 % mineral mass fraction), sulfides and phosphates, in addition to the clay and sand. Micas include "Muscovite", "Biotite" and "Glauconite", sulfides include heavy minerals like "pyrite", silicates like "zircon" and the only phosphate class of mineral was "apatite" (< 0.1% of mineral mass). There were no carbonates detected. In the clay lens, in addition to kaolinite, illite and smectite, chlorite and Berthierine were detected in small quantities (<0.2 % of total mineral mass).

3.1. Cementing Agents

Usually, the cementing agents in sandstones is "calcite" —which does not exist in the Viking core samples or is found in very small quantities. Calcite causes cementing by pore water ion concentrations precipitating onto the surface of the sand. When the precipitated calcite bridges two or more sand grains, it can act as a binding agent. Lack of calcite in the XRD analysis indicates a low level of "cementing" between the sandstone grains resulting in a more friable rock type. Clay minerals can sometimes contribute to grain cementing. However, in the presence of water, the clay dissolves in the water phase and then is less effective in cementing the sand grains. The other element that can act as a cementing agent is "smectite." It can contribute to increased strength of sandstones, but only when the core can dry over the course of time at surface conditions.

Chlorite does not usually act as a cementing agent but can precipitate around other neighboring minerals and add to the strength of the rock. As such, the current strength of the rock is due to the effective stresses developed during formation compaction, and over consolidation, rather than diagenetic cementation. The use of averaging techniques to calculate geomechanical properties (rock compliance and stiffness) from constituent minerals is valid from a physical point of view. No" tuning" factor should be used in addition to the average properties (i.e. bulk modulus) to account for cementing. However, as mentioned, the consideration of the impact of historical stress regime and stress path in the reservoir that has resulted in the current pore compressibility, frame compressibility and bulk compressibility being important in order to predict geomechanical properties.

4. METHODOLOGY

The main three methodologies in the workflow are: 1) XRD analysis 2) QEMSCAN analysis and 3) CT scan-based segmentation (based on Deep Learning). The methodologies can function independently, but if they are combined in the sequence that is mentioned, it can lead to the most reliable results.
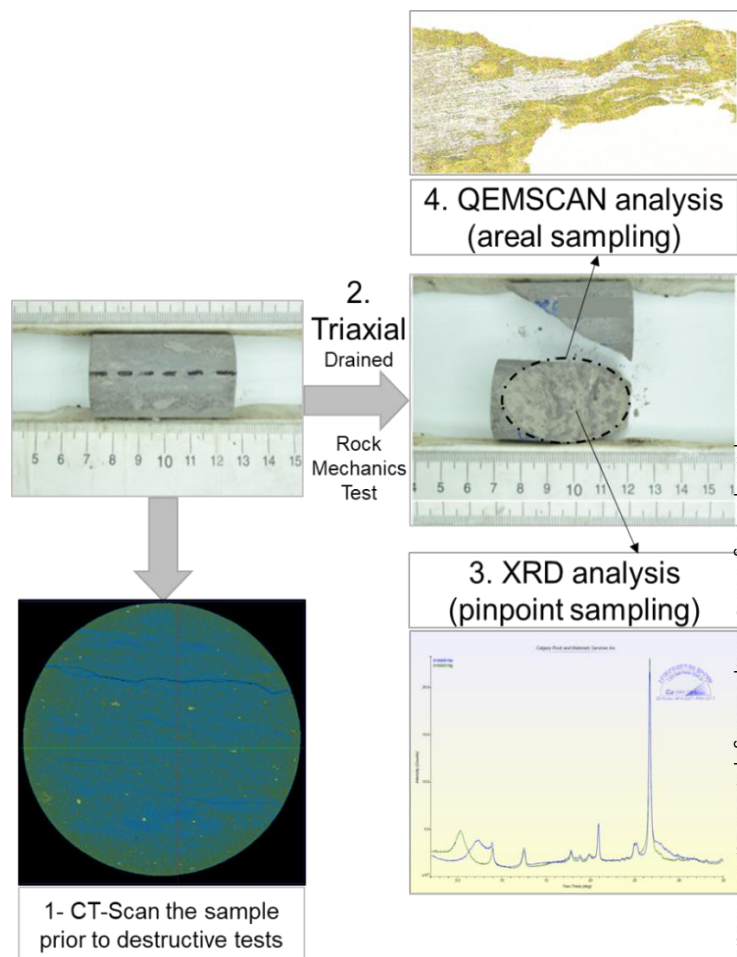

Fig. 4. Schematic of overall interactive workflow and methodology steps toward prediction of rock geomechanical properties. (images related to core sample ID #2).

4.1. XRD derived geomechanical properties

The XRD analysis is based on the Rietveld Refinement Method which was conducted on core samples from a Kerrobert area well cored in the Viking formation. The XRD analysis was conducted on all five core samples listed in Table 1. Each dot in the plots of Fig. 5 and Fig. 6 show one rock sample. The clay species were separated from the sand in the analysis using a cut-off grain size < 5 microns, and the reported mass fraction of quartz, K-feldspar, and plagioclase was taken from the bulk powder mixture analysis of the sand and the clay minerals.

The XRD results showed potassium feldspar exists in lower quantities than the other two types of feldspar minerals found in the Viking formation samples. As such, analyzing the rock strength based on the "quartz" portion alone due to its stiffness and cementing between quartz minerals will miss the strength contributions of the other stiff minerals. Therefore, the rock strength was plotted versus combined quartz and feldspar wt. %. Fig. 5 shows the combination of quartz, k-feldspar and plagioclase (constituents of the sand group) showed a relatively good and physically meaningful correlation. The larger the mass proportion of these minerals, the smaller the dynamic Poisson's Ratio and the larger the static Young's

Modulus, and the larger the bulk and dynamic moduli. Also, the larger the mass portion of these minerals, the larger the uniaxial compressive strength (UCS), and tensile strength.

Fig. 6 shows the relationship of geomechanical properties with respect to illite-smectite in the clay lens. The illite-smectite portion adversely affected the friction angle, uniaxial compressive strength and rock's cohesion, as indicated in the correlation plots.

Since there was only a small number of data points for the correlations, in both Fig. 5 and Fig. 6, the 95% confidence interval curves (note the 50% confidence interval in one plot) were constructed with 1000 iterations in order to provide an idea of reliability for the curves and the trends.

The 3-axis plots in Fig. 7 and Fig. 8 show the relative impacts of the clay and sand weight percentage on the dynamic and static Poisson's Ratio and Young Modulus of the core samples. Although there are some fluctuations on the surface plot, the overall trend and tendency of the surface plot indicates that the larger the sand weight % the larger the static and dynamic Young Modulus and the lower the Poisson's Ratio, and the larger the clay portion of the rock, the larger the Poisson's Ratio and the smaller the Young Modulus.
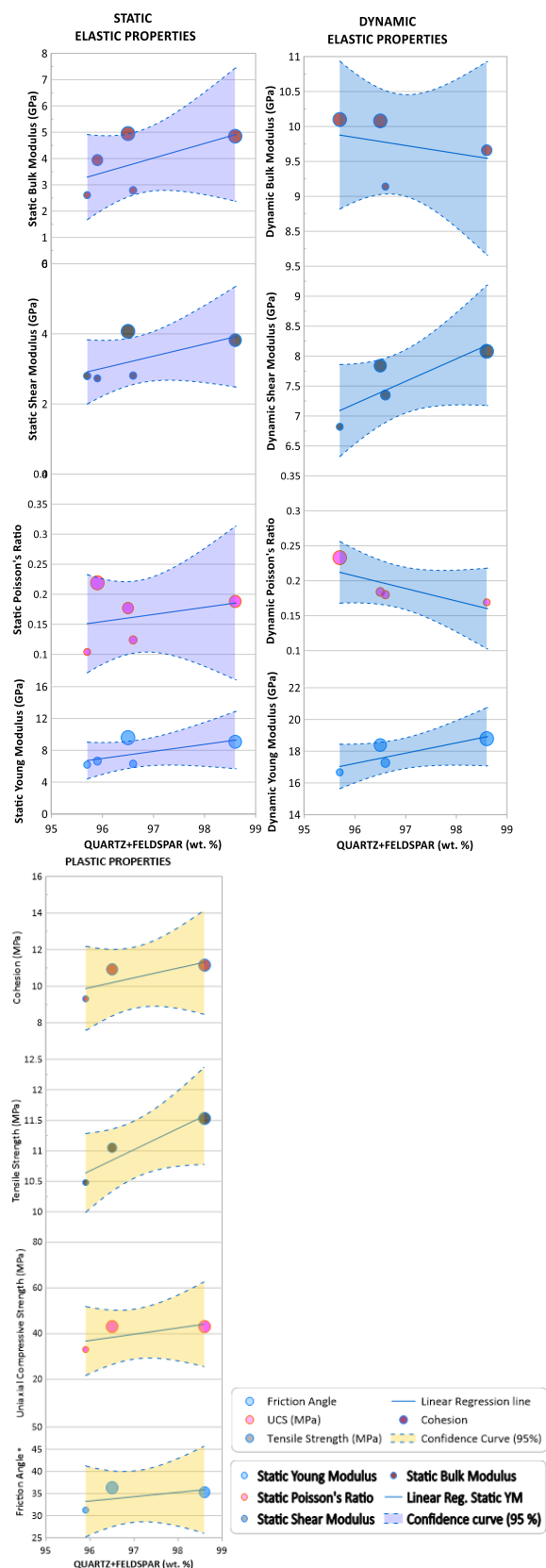

Fig. 5. Cross plot correlation of elastic (static and dynamic) and plastic geomechanical properties versus mineralogical composition of sand portion of the core samples.
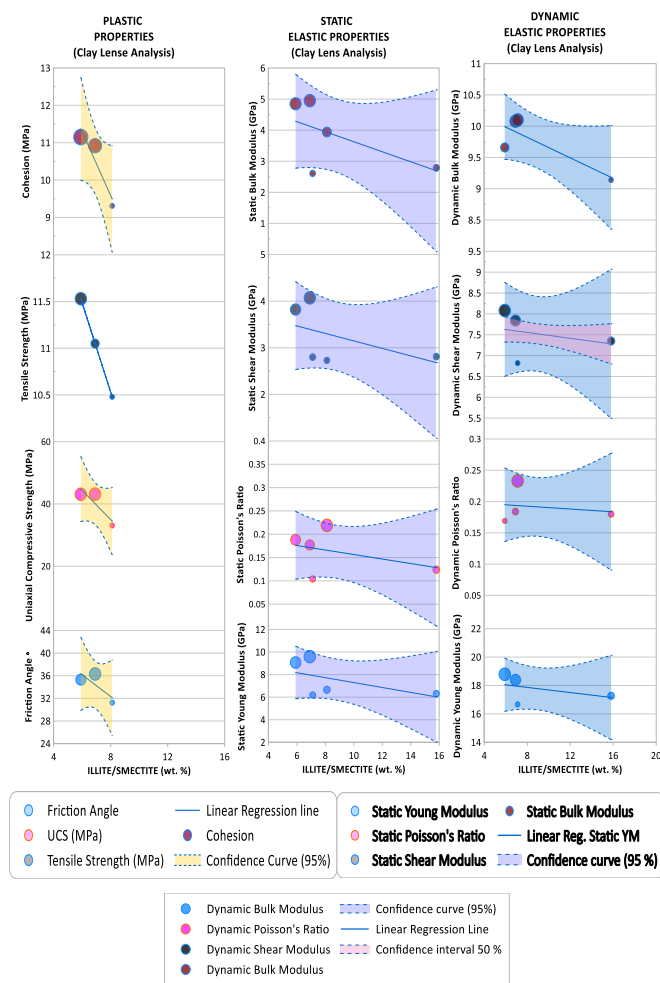

Fig. 6. Cross plot correlation of geomechanical elastic and plastic properties versus illite-smectite mass fraction of clay in the core samples.
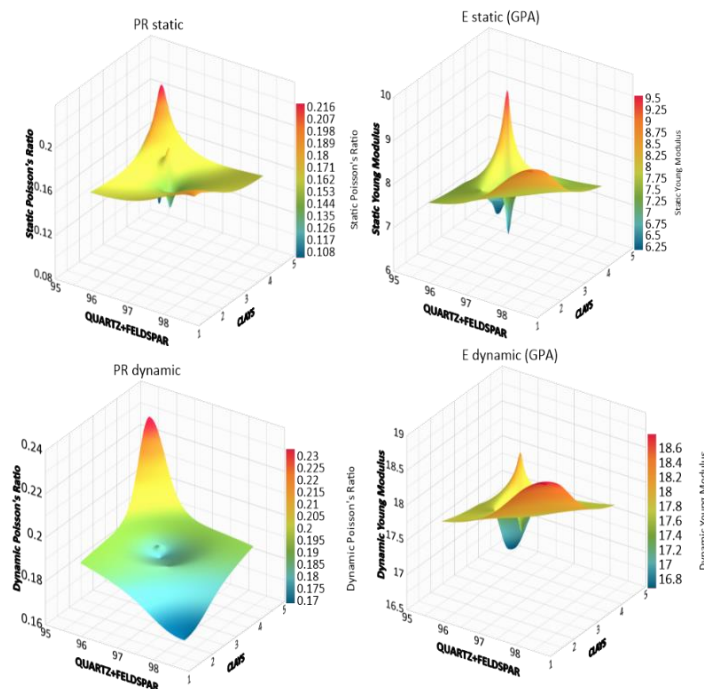
Fig. 7. Static and dynamic elastic properties obtained from triaxial rock mechanics tests, versus sand and clay mass fractions in the core samples.
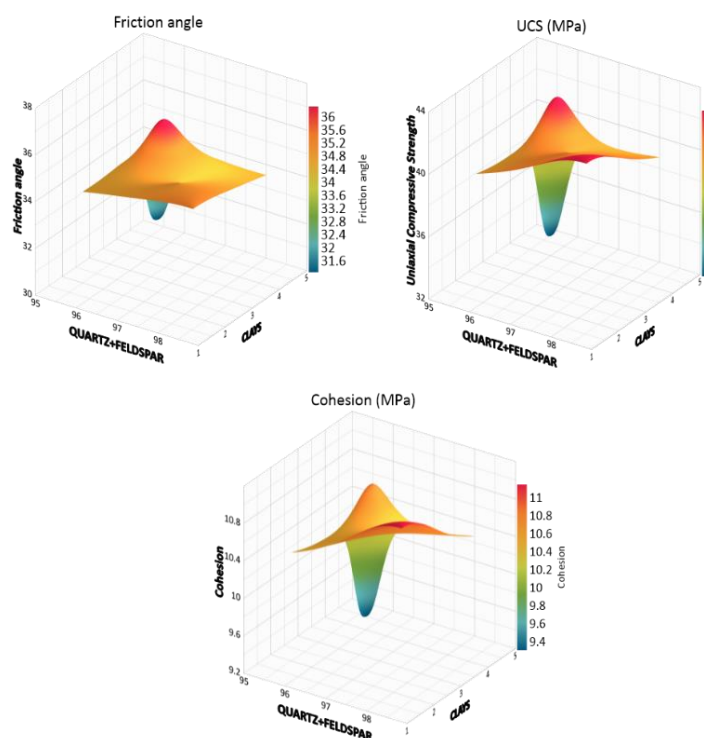

Fig. 8. Plastic (yield envelope) properties obtained from multistage triaxial rock mechanics testing, versus sand and clay mass fractions in the core samples.

4.2. QEMSCAN derived relationships

QEMSCAN analysis was performed after triaxial tests on the prepared thin section on the plane of failure of the five core samples. Results are shown in Fig. 9. At the plane of failure, both the thin section (thickness of 30 μm) and the wafer sample (200 μm) were collected for QEMSCAN analysis. The QEMSCAN was performed on the prepared

thin section, since it was closer to the plane of failure. In addition, the sample was thinner, and, due to the use of Canada balsam glue between the cover slip and the rock sample, it was easier to remove the cover slip and perform more accurate tests. The plane of failure was selected as the scan area since the rock showed this to be the weakest mineral surface and as such the mineral distributions and derived mechanical properties from this surface distribution are more representative of the rock yield envelope and stiffness. However, the area where the thin section was selected had some irregularities. It was not polished to a smooth surface in order to retain the original mineral distribution on the plane of failure and the intrinsic surface roughness. The irregularities resulted in the white areas shown in the Fig. 9 QEMSCAN images. The resolution for spot size scanning was 10 μm which is relatively good for the grain sizes and mineral maps of the Viking formation rocks being investigated. Nevertheless, if the groundmass of fine grains is smaller than the spot size, they will show as unclassified regions. Fortunately, in our case the unclassified regions are very minor in mass percentage. The other reason for unclassified areas was that the EDX/BSE characteristics of the regions were not within the range of known minerals in the database.
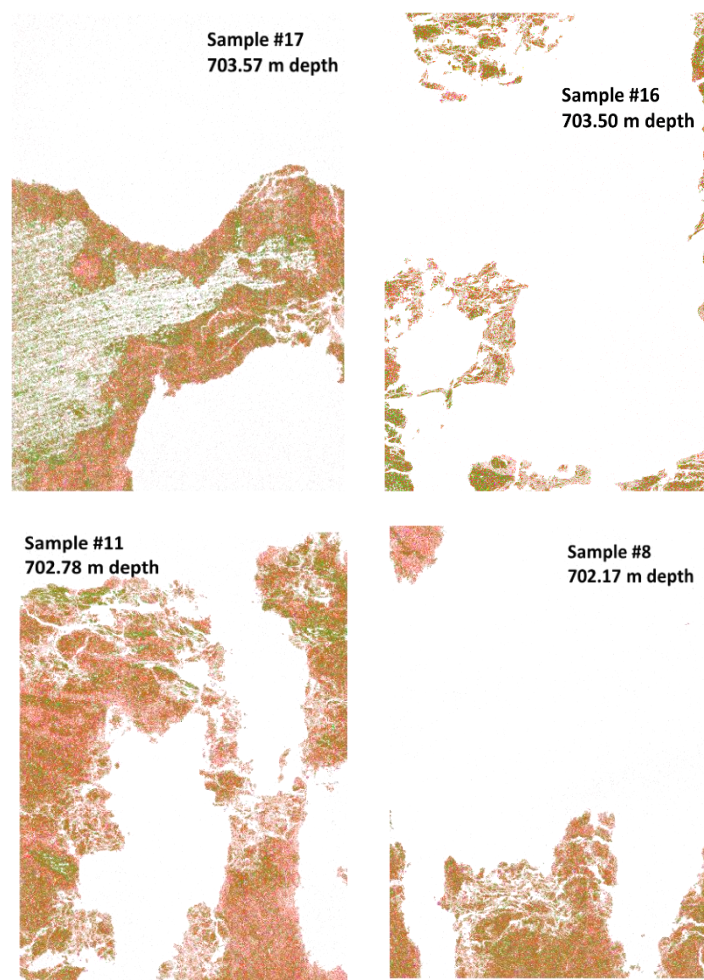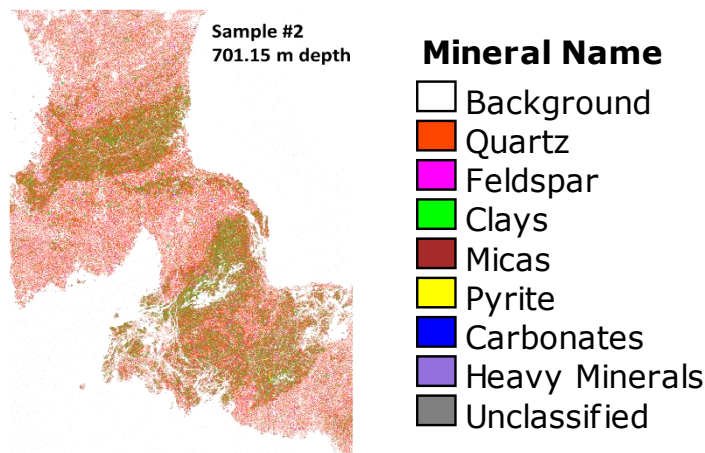
Fig. 9. QEMSCAN areal distribution of various minerals on the plane of failure (post-triaxial tests) for five different core samples.

In the QEMSCAN analysis, the mixed interbedded clays were not detected because of the overlap of elemental compositions with other clay group minerals. An important aspect of the QEMSCAN analysis is the sand and shale lithologies are not mineralogically distinct and discrete, there is no clear boundary between sandy and muddy clay zones, and the textures of each mineral phase is quite varied. This effect is a limitation in the averaging techniques and the image segmentation of sand and clay minerals in the core samples. Unfortunately, this is a characteristic of Viking formation rocks. Due to the erosional and depositional history of the deposits, the clay rich formations have migrated, and the clay fragments have mobilized throughout the sandy rocks resulting in their distribution being quite scattered (see Section 4.3.1). Chlorite (as mentioned in a previous section) can enhance the stiffness of the rock if it is associated with the deposition. Chlorite deposition was studied petrographically from thin sections but was not identifiable due to the fine-grained nature of the Viking formation rocks, and the chlorite can get easily intermingled with other clay group minerals. A scanning electron microscopy (SEM) test, can provide good insight on chlorite disposition in addition to the rock fabric and quantification of cementation volumes, but SEM examination was not within the scope of this work.

Table 2. Summary of QEMSCAN mineralogical composition mass %

Sample Depth	701.15 m	702.17 m	702.78 m	703.5 m	703.57 m
Minerals Mass %					
Sample ID	#2	#8	#11	#16	#17
Quartz	68.75	58.72	61.85	53.71	50.31
K-Feldspar	4.89	4.97	4.87	4.16	4.24
Plagioclase	6.87	8.88	8.26	9.95	12.03
Calcite	0.00	0.00	0.00	0.00	0.00
Dolomite	0.00	0.00	0.00	0.00	0.00
Siderite	0.02	0.00	0.00	0.01	0.00
Kaolinite	5.74	8.85	8.20	10.11	8.99
Berthierine	0.01	0.02	0.02	0.01	0.02
Illite	4.70	6.86	6.25	9.01	10.11
Smectite	7.51	9.64	8.90	10.85	11.45
Chlorite	0.09	0.11	0.08	0.08	0.14
Muscovite	0.54	0.67	0.63	0.64	0.88
Biotite	0.01	0.02	0.02	0.07	0.03
Glauconite	0.01	0.00	0.00	0.00	0.00
Pyrite	0.40	0.75	0.50	1.02	1.37
Rutile	0.02	0.01	0.02	0.01	0.01
Zircon	0.03	0.03	0.04	0.03	0.02
Apatite	0.11	0.09	0.08	0.03	0.06
Unclassified	0.32	0.37	0.30	0.31	0.33

As opposed to the XRD cross-plot against geomechanical elastic and plastic properties, the mass fraction and/or volume fraction of the mineral compositions obtained from QEMSCAN did not show a strong correlation and physically meaningful pattern with respect to the laboratory measured geomechanical properties. However, the plastic properties showed a physically reasonable trend with respect to sand mineral groups and clay mineral groups (Fig. 10). This means that the larger the sand portion and the lower the clay portion, the stiffer the rock properties in terms of the plastic envelope constitutive model properties such as Cohesion and Friction Angle. This was the case for both Uniaxial Compressive Strength and Tensile Strength of the rock.
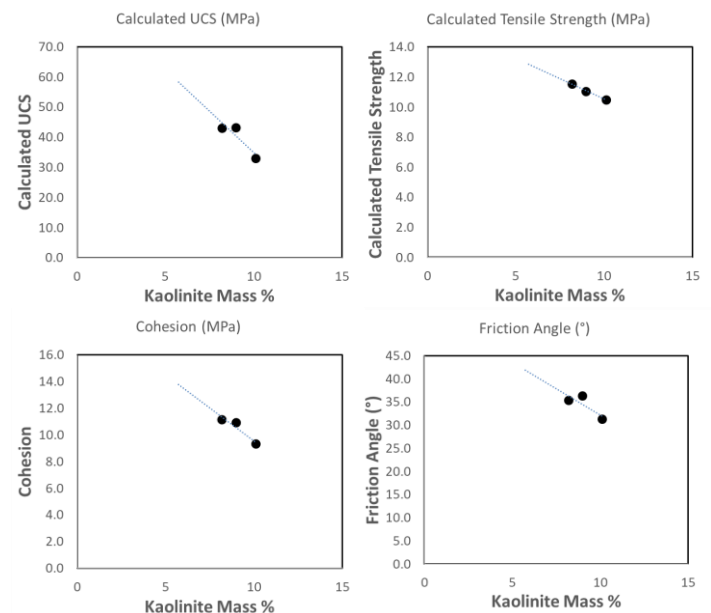

Fig. 10. Cross correlation between plastic (yield envelope) geomechanical properties and kaolinite % (obtained from QEMSCAN)

The only elastic property that was relatively correlating to the mass fraction of QEMSCAN derived mineral compositions was the hydrostatic bulk modulus of the rock (Fig. 11 and Fig. 12). This could be due to the fact that the areal distribution of the minerals alone is not sufficiently representative for the characterization of the overall geomechanical properties, i.e. the entire volume mineralogy accounts for the rock compliance or stiffness. In addition, the irregularities on the rough fracture surface left a large void and subsequently a large background space, where the mineral compositions were not analyzed and are therefore unknown. Nevertheless, the mineral distributions of the various samples helped to obtain a good estimate of average sand and clay bulk and shear moduli of the core samples (Table 2).

Although a number of core samples in both the XRD and QEMSCAN cross correlation were not large enough to obtain a reliable trendline, some of the correlations were sufficiently strong that the confidence interval matched the trendline exactly, such as the Kaolinite Mass %. Also, the physical explanation behind the behaviour of the curves with respect to mineralogical composition provides a good insight on the existence of a correlation for each formation that can be derived quite accurately where there is an abundance of data, such as drill cut data along a horizontal wellbore, where these minerals are present.
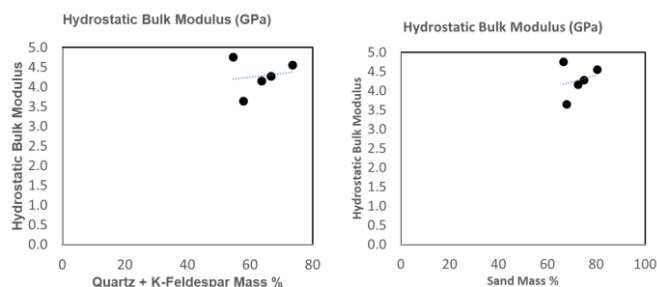

Fig. 11. Cross correlation between sand mass% (obtained from QEMSCAN) and hydrostatic bulk modulus of the rock
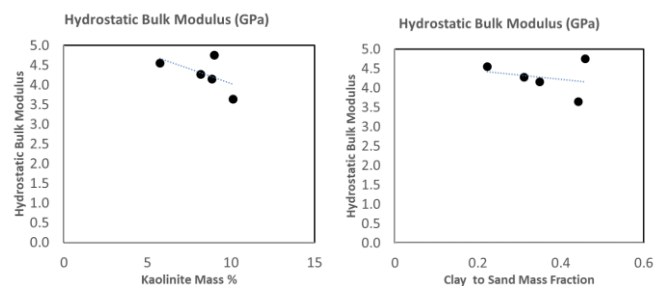

Fig. 12. Cross correlation between hydrostatic bulk modulus of the rock and kaolinite mass% and clay mass % (obtained from QEMSCAN)

In all figures, the sand group includes quartz, K-feldspar and Na-feldspar, and the clay group includes kaolinite, illite, smectite.

4.3. CT-SCAN derived geomechanical properties

All of the core samples were CT scanned prior to any destructive tests (such as triaxial tests) and before the XRD and QEMSCAN analysis was performed on them. Table 3 summarizes the important technical specifications of the CT scanning technique, which was conducted on 1" diameter core plugs.

Table 3. CT Acquisition Technical Specification

Property/Attribute	Value
Tube Voltage	100 kV
Current	200 µA
Detector pixel pitch	[200 x 200] microns
Distance of tube to detector	1122.763 [mm] (FDD)
Distance of tube to object	225.249 [mm] (FOD)
Effective pixel pitch	0.04012 [mm]

The XRD and QEMSCAN analysis helped tune the CT derived geomechanical data and provided identification of the constituent minerals in the rock. However, the CT based geomechanical characterization is an independent method. The key predictive method for estimation of geomechanical properties using CT scans is based on segmentation, which was done using Machine Learning based algorithms.

4.3.1. Segmentation and Digital Rock Physics

Segmentation of data (voxels in this case) refers to voxel classification in an object (rock matrix in this case), and the output of segmentation is a label for each voxel cluster of a particular mineral density range, i.e. x-ray absorption thresholding range. This partitions the object into multiple segments, each representing a different mineral. The voxel fraction for each segmented mineral is the volume fraction of that mineral relative to the total object volume, which is the core plug volume in this case. As such, the creation of a segmented core volume representing the different minerals based on x-ray absorption ranges is the initial step in this workflow.

The main objective of segmentation in this work is to decompose the bulk volume into two separate portions: 1) sand rich portion 2) clay rich portion. Based on the depositional history of the Viking formation, visual examination of the core sample and QEMSCAN results shown in Fig. 9, the sand and clay portions of the rock are not nicely separated, but rather the sand and clay minerals are highly interbedded. This made the thresholding segmentation of the two mineral portions difficult, especially because "global thresholding" was used for analysis.

The criterion to separate the sand rich portion from the clay rich portion were a) the inverse histogram of x-ray intensity that is an indication of minerals' atomic number and density, b) location and distribution of cracks with respect to the segmented volumes and c) repeatability and

consistency of segmented areas on a (circular) cross section throughout the volume of the core sample. Based on XRD and QEMSCAN analysis of results on the five selected core samples, the sand mineral constituents are considered as "Quartz and Feldspar" and the clay dominated constituents are considered as "Kaolinite, Illite and Smectite". Since the constituent atoms in the clay minerals segment have larger atomic numbers with higher x-ray absorption, they appear "whiter" in the CT images due to the inverse histogram. The larger the atomic number of the minerals, the brighter they will show in the CT images. As such the solid white spots on the CT images are interpreted as iron pyrite, which is atomically dense mineral component naturally found in the Viking formation cores. The darker regions in the image are classified as "sandy" portions since the minerals have smaller atomic numbers with less x-ray adsorption. Another indicative factor is the existence of cracks and microcracks in the core plugs which have developed either in the reservoir in-situ conditions, or due to core cutting and subsequent extraction at the surface (unloading), which in both cases is more likely to occur in the mechanically more brittle material characterized by larger Young Modulus and smaller Poisson's Ratio. In this case, the brittle and darker material is sand.

repeatable and reliable. The first steps in the segmentation method is selecting a random cross section where the intensity histogram is very distinctive, i.e. the density discrimination of the minerals is more pronounced, and using this histogram threshold selection check on the consistency of the (classification) segmentation throughout the entire volume of the rock at various 2D planes to ensure consistency (x-z in this case that represent a circular cross section).
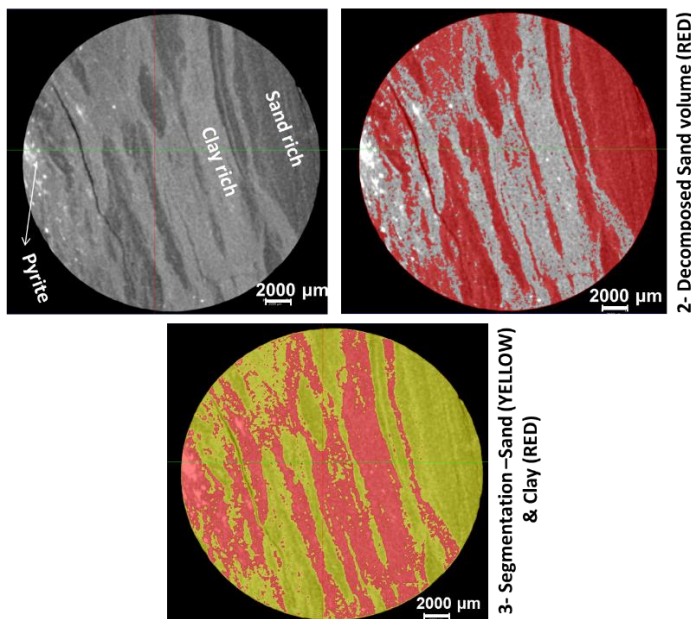
Fig. 13. Segmented sand (rich) and clay (rich) portion of core plug #2.

As can be seen in the images (Fig. 13), the micro-fractures have developed in the darker regions indicating sand. Fig 14 summarizes the segmentation workflows illustratively on core plug 2. The segmentation algorithm uses the histogram intensity, which has a direct relationship with the physical properties of the minerals, such as the atomic number and bulk density. Fora given set of CT scan parameters (power and time) the relative absorption of each mineral in the object is the same, and therefore the digital rock physics segmentation workflow is physically

1- Original CT-Scan 3D display
(Smoothing & Pre-Processing)

2- Segmentation
Decompose Clay Lens &
Assign Properties (Based on color intensity
historgram, atomic number &
crack distribution)

3- Segmentation
Combine Sand rich portion
(purple) and
Clay rich lens (green)

4- Volume Fraction
Based on segmented
voxel volumes

Fig 14. Illustrative Machine Learning based segmentation workflow, post CT scanning (sample # 2).

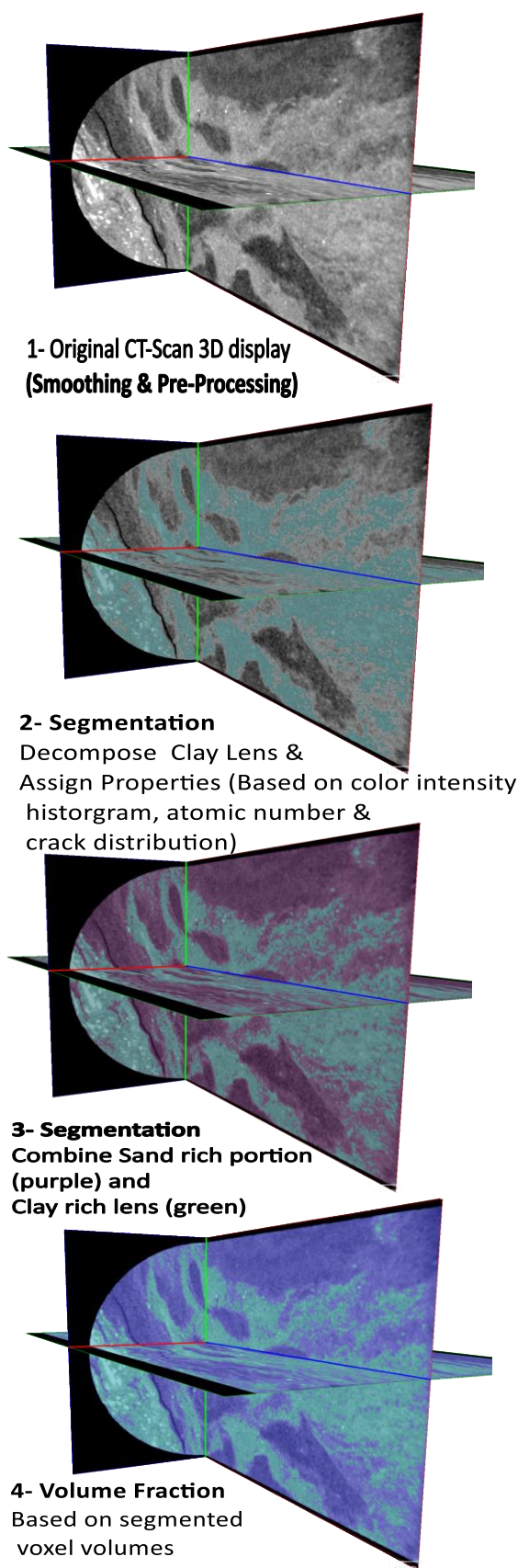Once the segmentation is complete, each voxel in the core plug image has been designated as a volume of either sand or clay rich materials. The next step is to calculate the total number of voxels in each segment portion's and divide by the total number of voxels in the core plug to obtain the individual volume fraction of sand rich and clay rich phases.

The segmentation methodology used in this work was the "Interactive Overlay Threshold" (PerGeos, 2019), which selects values within a specified histogram threshold range for an image and is one of the global thresholding techniques. The threshold ranges can be selected interactively, and every interval (upper and lower value of spectrum) corresponds to a specific range in the image's histogram. In our case, the higher threshold values correspond to clay (and pyrite) and lower threshold values refer to sand.

One downside of this technique is that thresholding the image based on the histogram intensity, in some cases, can lead to incorrectly assigned voxels, where the peaks from differing mineral phases overlap in the histogram (regardless of the number of discrete phases). Another disadvantage of global thresholding is that it fails if the image is noisy, or if the background intensity (clay mineral in this case) varies significantly, or if the contrast between the "object" sand mineral and the "background" clay mineral is not high (Rogowska, 2009).

In our study, there was not a sharp discrete phase segregation between the sand rich (light grey) and clay rich (dark grey) portions in the CT images. Because of the uncertainty of the segmentation, an upper bound and lower bound of sand volume fraction was calculated to predict geomechanical properties.

Global segmentation which was used in this work, is one of the most basic and intuitive approach that requires at least two peaks (for binary segmentation) in the image intensity histogram.

The key step is assigning the right threshold (intensity value) in a fashion that all voxels that fall under the assigned threshold constitute one phase. Although this work used manual threshold selection at the 3D level, there are some automated choices of threshold by conducting a binormal fit to the two-peak histogram and selecting the interpeak minimum. It is possible to apply several individual thresholds (multi thresholding), but when the number of regions or phases increase, it will be difficult to select thresholds. The most basic thresholding function that outputs a binary image, can be defined as follows (Rogowska, 2009):

$$G(x,y,z) = \begin{cases} 1 & if\ (x,y,z) > T : object \\ 0 & if\ (x,y,z) \leq T : background \end{cases} \quad (1)$$

The reason that this approach is called "global", is that there is only one threshold for the entire (core plug) image

that is based on the image histogram. Alternatively, there is dynamic or adaptive thresholding that has two main characteristics: they are local, meaning that thresholding is localized on a region of images, and the thresholds are independent for each pixel (Rogowska, 2006)

It may be possible that once the Deep Learning algorithm is working well for several real cases, and was calibrated against the real laboratory measured data (triaxial rock mechanics test), the segmentation algorithm and script can be trained to predict additional rock sample properties without having to run destructive tests on them.

4.3.2. Averaging Techniques and Mixing Laws (Effective elastic moduli)

In order to know the effective elastic moduli of a mixture of solid grains and the pore space that connects them, one needs to know: 1) volume fraction of different phases (constituent minerals), 2) elastic moduli of each phase, and 3) the geometric distribution of each component or phase (Mavko et al., 2014). Geometric details are usually the most difficult to determine and missing in most analysis. As such, the effective moduli of the mixture of grains and pores (where geometric distributions are unknown) will have a range: an upper bound and a lower bound, rather than a precise number. The bounds are formulated based on extreme geomechanical distribution of the rock compositions. There are several well-known mixing laws such as: Hashin-Shtikman (1963), Hashin-Shtikman-Walpole (1966), Voigt (1910) and Reuss (1929). These averaging techniques share the common assumptions that both the rock and the constituent minerals of the rock are isotropic, linear and elastic.

The physical assumption and mechanical boundary conditions behind the Voigt bound, is that both grains and fluid experience the same external strain due to an external hydrostatic loading, and that is why the Voigt bound is sometimes called the "isostrain average", as it provides the ratio of the average stress (confining stress σ_c) to the average strain (ϵ_v) in an isostrain condition. As such the Voigt bound is an upper bound for the bulk modulus.

$$M_V = \sum_{i=1}^{N} f_i M_i \qquad (2)$$

On the other hand, the Reuss bound is a lower bound and is sometimes called "isostress" average, as it provides the ratio of the average stress to average strain when all constituents and pore fluid experience the same "stress".

$$M_R = \sum_{i=1}^{N} \frac{f_i}{M_i} \qquad (3)$$

In both Reuss and Voigt bounds, f_i refers to the volume fraction of the ith phase and M_i is the elastic modulus of phase i. M_i in both Voigt and Reuss bounds can be replaced by either bulk modulus (K) or Shear Modulus (G), and the other elastic properties should be calculated from these two sets of known values (Mavko, 2014).

Physically speaking, the Reuss average represents the effective moduli if a suspension (solid gains in a liquid or gas bubbles in liquid) (Fjaer, 2008), or the moduli of shattered materials where the solid particles are surrounded by pore fluid (Mavko, 2014). The Voigt bound (upper bound) is most appropriate for a rock with low porosity (Fjaer, 2008), but in contrast to the Reuss bound that takes into account the real physics, the real isotropic mixtures can never be as stiff as the Voigt bound (Mavko,2014), except for single phases.

The arithmetic average of Voigt and Reuss bounds was presented by Hill (1952), and is expressed as,

$$M_{VRH} = \frac{M_R + M_V}{2} \qquad (4)$$

and is referred to as Voigt-Reuss-Hill average, which is an "estimate" of the modulus, rather than the allowable range.

The Hashin-Shtrikman approach (1963) provides a narrower range of the bound compared to the Voigt and Reuss bounds, which are very wide. Also, Hashin-Shtrikman's bounds are less dependent on the distribution of compositions, compared to the Voigt and Reuss.

$$K^{HS\pm} = K_1 + \frac{f_2}{\frac{1}{(K_2-K_1)} + \frac{f_1}{(K_1+\frac{4}{3}G_1)}} \qquad (5)$$

$$G^{HS\pm} = G_1 + \frac{f_2}{\frac{1}{(G_2-G_1)} + \frac{2f_1(K_1+2G_1)}{5G_1(K_1+\frac{4}{3}G_1)}} \qquad (6)$$

In equations (5) and (6) above, K_1 and K_2 refers to the bulk modulus of each phase and G_1 and G_2 refers to the shear modulus of each phase, and the individual phase volume fractions are denoted by f_1 and f_2. The (+) sign refers to the upper bound of the modulus and is obtained when the stiffest material is index (1) in the equation and the lower bound (−) is computed by replacing the softest material by index (1) in the formulation.

An extension to Hashin-Shtrikman bounds were provided by Walpole (1966) to account for the fact that a composition with the larger bulk modulus does not necessary have the larger shear modulus, and the material with the smaller bulk modulus does not always have the lower shear modulus (such as the case of mixed calcite and quartz). These modified expressions are shown below in equations (7) and (8).

$$K^{HSW\pm} = K_1 + \frac{f_2}{\frac{1}{(K_2-K_1)} + \frac{f_1}{(K_1+\frac{4}{3}G_m)}} \qquad (7)$$

$$G^{HSW\pm} = G_1 + \frac{f_2}{\frac{1}{(G_2-G_1)} + \frac{f_1}{[G_1+\frac{G_m}{6}(\frac{9K_m+8G_m}{K_m+2G_m})]}} \qquad (8)$$

Where K_m and G_m are either maximum bulk and shear moduli among all rock compositions (upper bound HSW)

or are minimum bulk and shear moduli among all rock's mineral compositions (lower bound HSW).

In our workflow, the phases in all the averaging techniques were "clay" and "sand", and their volume fractions were provided by the segmentation of CT scanned core images. The methodology in our case study can be summarized as follows for each core sample:

1. Compute f_i or x_i for all mineral compositions:

   - Lump the sand minerals (such as quartz, feldspar) into the sand moduli, and clay compositions (such as kaolinite, illite, smectite) into the clay moduli of the rock.

2. Compute K_{sand} , K_{clay}, G_{sand}, G_{clay}:

   - Deploy Reuss and VRH averaging techniques on QEMSCAN derived mineralogy to calculate average sand and clay stiffness and compliance.

   - Note[1]: Individual constituents geomechanical properties are available and are physically well known.

   - Note[2]: Where QEMSCAN or XRD results are not available, use the literature average values for sand and clay bulk and shear moduli.

3. Compute f_{sand}, f_{clay}:

   - Calculate sand and clay volume fractions from segmentation techniques on the CT imaged core samples.

4. Compute K_s: Use all mixing laws to compute effective intrinsic bulk and shear modulus of each core sample.

5. Include the effect of pore structure (pore compressibility, $K_\emptyset$) as well as fracture/crack inclusion in the background matrix if known on bulk and shear modulus values.

6. Compare the computed results against drained (dry) bulk modulus ($K_{drained}$) obtained from triaxial rock mechanics testing in the laboratory.

Drained bulk modulus can be calculated directly from a triaxial drained test by combining laboratory measured static Young Modulus (E) and Poisson's Ratio (v) ($K = \frac{E}{3(1-2v)}$) or from hydrostatic rock mechanics testing. The notation for bulk compressibility (β) is provided by Zimmerman (1991) and the signs are chosen by assuming the compressibility values are positive when tensional stresses are positive.

$$K_{drained} = V_b \frac{\partial \sigma_c}{\partial V_b}\big|_{\sigma_p} = \frac{1}{\beta} \qquad (9)$$

In equation (9), V_b is the bulk volume of the core sample, σ_c is the confining hydrostatic stress, and the modulus is calculated under constant pore pressure σ_p (requirement of drained test).

It must be noted that the solid grain modulus K_s is different than dry pore space modulus $K_\emptyset$ (reciprocal of pore compressibility) and along with pore filling fluid modulus (K_f) contributes to bulk modulus(Zimmerman 1991).

$$\frac{1}{K_{drained}} = \frac{1}{K_s} + \frac{\emptyset}{K_\emptyset} = \frac{1}{(1-\emptyset)}\left(\frac{1}{K_s} + \frac{\partial \emptyset}{\partial \sigma_c}\right) \qquad (10)$$

In our study, based on the mineral compositions provided in Table 2 , $K_{sand} \approx 36.5\ GPa$, and $K_{clay} = 2.396 - 3.2\ GPa$ depending on the core sample's individual composition.

Table 4. CT-scan derived sand volume fractions of sand and clay with computed moduli of each phase.

Sample #	f_{sand} Segmentation	K_{fluid} (GPa)	K_{sand} (GPa)	K_{clay} (GPa)	G_{sand} (GPa)	G_{clay} (GPa)
2	0.6343	2.2	36.5	3.493	35	3.058
7	0.6503	2.2	36.5	3.676	35	3.2
8	0.4882	2.2	36.5	3.303	35	2.909
11	0.7010	2.2	36.5	3.291	35	2.9
16	0.4887	2.2	36.5	3.376	35	2.967

Table 5 summarizes the Voigt and Reuss bulk moduli of five samples based on the segmented sand fractions derived from CT scanned images. The sand fraction values in Table 5 are the average of upper and lower sand fractions obtained from the segmentation.

Table 5. Digitally computed rock bulk moduli from segmentation techniques using VRH mixing laws.

Sample #	f_{sand} CT-Scan segmentation	K_{Reuss} Lower Bound	K_{Voigt} Upper Bound	K_{VRH} Voigt-Reuss-Hill
2	0.6343	6.0330	21.5079	13.7704
7	0.6503	6.3356	22.0219	14.1788
8	0.4882	4.8562	17.2369	11.0466
11	0.7010	6.4387	23.3690	14.9038
16	0.4887	4.9286	17.2821	11.1053

Table 6.Digitally computed rock bulk moduli from segmentation techniques using Hashin-Shtrikman mixing laws.

Sample#	f_{sand} CT-scan segmentation	K^{HS-} Lower Bound	K^{HS+} Upper Bound	$K^{HS\pm}_{average}$
2	0.6343	11.5627	20.3674	15.9650
7	0.6503	12.4048	21.0566	16.7307
8	0.4882	8.1190	15.3990	11.7590
11	0.7010	13.0433	22.7112	17.8773
16	0.4887	8.2667	15.4702	11.8684

4.3.3. Inclusion if impact of porosity and cracks

As previously mentioned, the inclusion of porosity and pore structure compressibility (modulus) decreases the bulk and shear modulus of the rock (Eq. (10)). In this part of the study, a micro-CT scan was not conducted. Therefore, the distribution of grains with respect to each other and pore space is not known. When a distribution of various mineral grains is not known, and the use of averaging techniques considers the extreme geometric distribution, i.e. homogeneous, other methods must be used to incorporate the impact of microstructure. One method that can be used is the concept of critical porosity. The critical porosity is the porosity above which the grains (compositions) will no longer be in contact with each other and there will be no frame or intrinsic modulus. The value for critical porosity for simple cubic packing is 0.476 and for random packing is 0.36 and for clean sand is about 0.4. In this study, the critical porosity was considered to be $\emptyset_c = 0.4$. Nur et al. (1995) related this effect to a straight line that can explain the frame modulus versus porosity in the simplest form:

$$K_{drained} = K_s(1 - \frac{\emptyset}{\emptyset_c}) \qquad (11)$$

$$G_{drained} = G_s(1 - \frac{\emptyset}{\emptyset_c}) \qquad (12)$$

Where K_s , and G_s are intrinsic solid bulk and shear moduli respectively, $\emptyset$ is porosity and $\emptyset_c$ is the critical porosity. It is obvious that at zero porosity, the dry bulk modulus is equal to the grain material modulus. An alternative form of the equation was provided by Kr5ief et al. (1990):

$$K_{drained} = K_s(1 - \emptyset)^{\frac{3}{1-\emptyset}} \qquad (13)$$

$$G_{drained} = G_s(1 - \emptyset)^{\frac{3}{1-\emptyset}} \qquad (14)$$

Table 7.Inclusion of porosity and critical porosity effects (by use of Nur et al approach) on the final digitally calculated bulk moduli of five core samples

Nur Sample#	$K_{drained}$ VRH mixing law	$K_{drained}$ Reuss mixing law	$K_{drained}$ HS^+ mixing law	$K_{drained}$ HS^- mixing law	$K_{drained}$ $HS^{average}$ mixing law
2	9.2474	4.0514	7.7648	13.6775	15.965
7	9.5216	4.2546	8.3303	14.1404	16.7307
8	7.4182	3.2611	5.4523	10.3410	11.7590
11	10.009	4.3238	8.7591	15.2515	17.8773
16	7.4577	3.3097	5.5514	10.3889	11.8684

Table 8. Inclusion of porosity and critical porosity effect (by use of Krief et al. approach) on the calculated bulk moduli of five core samples

Krief Sample#	$K_{drained}$ VRH mixing law	$K_{drained}$ Reuss mixing law	$K_{drained}$ HS^+ mixing law	$K_{drained}$ HS^- mixing law	$K_{drained}$ $HS^{average}$ mixing law
2	9.9501	4.0514	8.3549	14.7169	11.5359
7	8.7169	4.2546	7.6263	12.9454	10.2859
8	6.3172	3.2611	4.6430	8.8062	6.7246
11	12.100	4.3238	10.5900	18.4389	14.5143
16	7.1265	3.3097	5.3049	9.9275	7.6162

Fig. 15 provides an example of one of the averaging techniques that provided a relatively close match between CT scanned image segmentation data and the laboratory measured moduli. There are one or two cores (i.e. sample #11) among the five cores that contained a large amount of noise, and smoothing algorithms and artifice removal did not help to improve the data. Consequently, the trend of sand volume fractions was inconsistent with increasing values of bulk moduli. It is hoped that the development and use of new segmentation techniques and algorithms can improve the CT scanned core data derived results.
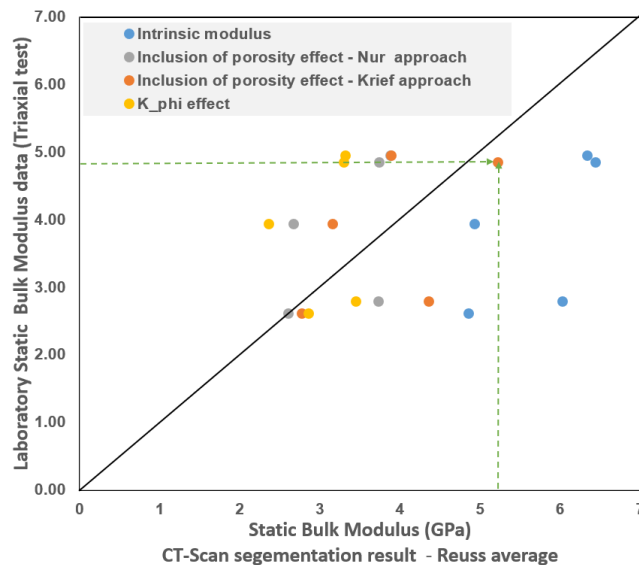

Fig. 15. comparison of computed bulk modulus from CT-scan non-destructive test versus laboratory derived drained static bulk modulus.

OTHER CONSIDERATIONS

Other factors that impact the rock moduli evaluation and needs to be taken into account are: rock compaction (consolidation and over-consolidation ratio of rock), and inclusion of micro and mini-fractures, and cracks in the rock samples. Use of the Küster method is suggested for inclusion of cracks, if the crack and microfracture density and distribution in the rock is known. Advanced smoothing and noise removal and artifact removal in the CT images can improve the results. Also performing

micro-CT-scanning and SEM examinations can provide the mineral grain geometrical distributions, which are physically important and can be mathematically included in the digital techniques for evaluation of the rock properties.

CONCLUSION

A workflow including XRD, QEMSCAN and CT-SCAN examinations was provided to predict the geomechanical properties of the rocks in a non-destructive mode. The tests were conducted on the core samples of a Kerrobert area well drilled and cored in the Viking formation. Both XRD and QEMSCAN tests were performed at the plane of failure (rock shear fracture surface in triaxial tests). The XRD analysis and results provided a relatively good correlation for estimating the geomechanical properties by knowing the rock mineral constituents. QEMSCAN analysis and the constituents' weight (and volume) fractions showed a relationship only with hydrostatic bulk modulus of the rock. However, Kaolinite weight percentage showed a physically meaningful trend with uniaxial compressive strength, friction angle and cohesion of the core samples.

The XRD, quartz wt. % alone was not sufficient to find a physically meaningful correlation with the static and dynamic geomechanical properties. However, the combination of quartz, k-feldspar and plagioclase obtained from XRD showed a good and physically meaningful correlation. XRD results showed that the larger the sandstone content the larger the rock strength, rigidity and brittleness (larger Young's Modulus and smaller Poisson's Ratio).

A new methodology was provided to estimate geomechanical properties from 3D CT scan images of the core sample bulk volumes. The methodology used a segmentation technique, combined with a few different mineral mixing laws to calculate the elastic properties, such as bulk modulus. Validation of the method was established by comparing the results of laboratory triaxial tests of the bulk modulus (post CT scanning) and segmentation derived moduli values. The sand and clay volume fractions, obtained from segmentation and digital rock analysis, were used with well-known mineral mixing laws to evaluate the grain and intrinsic rocks' moduli. After inclusion of pore structure modulus, the results were compared with drained (dry) bulk modulus of rocks that were obtained in the laboratory. Some of the mixing laws combined with the segmentation technique showed good correspondence to the laboratory measurements. The methodology showed that geomechanical properties of rocks can be predicted digitally without performing destructive tests. The methodology and algorithms will need to be tuned for each different "formation" with specific and usually unique mineral constituents of the formation rock.

ACKNOWLEDGEMENT

REFERENCES

1. Hashin, Z., Shtrikman, S. 1963. A variational approach to the elastic behaviour of multiphase materials.*J. Mech. Solids* 11, 127–140.
2. Hill, R. (1952). "The elastic behavior of crystalline aggregate". *Proc. Physical Soc. London* A65, 349–354.
3. K.Hosseini, B., Eaton, DW., 2018. Fluid flow and thermal modeling for tracking induced seismicity near the Graham disposal well, British Columbia, Canada. *In proceeding of SEG Technical Program Expanded Abstracts 2018 (ISSN (Online): 1949-4645)*. DOI: 10.1190/segam2018-2996360.1
4. Katz, D., Jung, M., Canter, L., et al.,2016. Mineralogy Derived Brittleness from the Qemscan: Niobrara Case Study. *SPE Low Perm Symposium*, Denver, Colorado, U.S.A., 5-6 May. https://doi.org/10.2118/180251-MS
5. Koohmareh Hosseini, B., Chalaturnyk, RJ., 2014. Streamline-based Reservoir Geomechanics Coupling Strategies for Full Field Simulations, *European Conference for Mathematics of Oil Recovery, ECMOR-XIV 2014*, Italy, DOI: 10.3997/2214-4609.20141899.
6. Krief, M., Garar, J., Stellingwerff, J., and Ventre, J. 1990. A petrophysical interpretation using the velocities of P and S waves (full-waveform sonic). *The Log Analyst*, 31, November, 355-369.
7. Kuster, G.T., and Toksöz, M.N. 1974. Velocity and attenuation of seismic waves in two-phase media: Part I. theoretical formulations: *Geophysics*, 39, 587-606.
8. Mavko, G., Mukerji, T., Dvorkin, J.2014. The Rock Physics: tools for Seismic Analysis in Porous Media *Handbook, 2nd ed. CAMBRIDGE University Press*.
9. Nur, A., Marion, D. & Yin, H. 1991.Wave velocities in sediments, in Shear Waves in Marine Sediments, pp. 131–140, eds Hovem, J.M. et al., Kluwer, Dordrecht.
10. Nur, A., Mavko, G., Dvorkin, J. & Galmudi, D., 1998. Critical porosity: a key to relating physical

properties to porosity in rocks, *The Leading Edge*, 17, 357–362.

11. PerGeos Software User's Guideline. 2019. *ThermoFisher Scientific*.

12. Reuss, 1929. Berechnung der Fließgrenze von Mischkristallen auf Grund der Plastizitätsbedingung für Einkristalle. Z. *Ang. Math. Mech.*, 9, 49-58.

13. Rogowska, J., 2006. Digital Image Processing Techniques for Speckle Reduction, Enhancement, and Segmentation of Optical Coherence Tomography (oct) images. DOI : 10.1016/B978-012133570-0/50013-5. *Academic Press*, Pages :305-329, 329a.

14. Rogowska, R. 2009. *Handbook of Medical Image Processing and Analysis* (Second Edition). Page 73-90.

15. Saxena, N., and Mavko, G. 2016. Estimating elastic moduli of rocks from thin sections: Digital rock study of 3D properties from 2D images. *Comput. Geosci.*, vol.88, pp. 9–21, Mar. 2016.

16. Saxena, N., Mavko, G., Hofmann, R., and Srisutth iyakorn, N. 2017. Estimating permeability from thin sections without reconstruction: Digital rock study of 3D properties from 2D images," *Comput. Geosci.,* vol. 102, pp. 79–99, May 2017.

17. Settari, A., Warren, G.M. 1994. Simulation and field analysis of waterflood induced fracturing. In: *Proc. Eurock* '94, Delft, pp. 435–445.

18. Vaisblat, N., Rangriz Shokri, A., Ayranci, Harris, N., and Chalaturnyk, RJ. Significance of Rock Compositional Control on Geomechanical Properties and Hydraulic Fracturing of the Montney Formation, Western Canadian Basin. 2019.URTEC-*198199-MS*.

19. Voigt, W. (1910). Lehrbuch der Kristallphysik. *Teubner, Leipzig*.

20. Zimmerman, R.W. (1991). Compressibility of Sandstones. *Elsevier Science Publishers*, B.V., The Netherlands.